

Off-the-Grid Sparse Imaging by One Dimensional Sparse MIMO Array

Li Ding, Shuxian Wu, Xi Ding, Ping Li and Yiming Zhu

Abstract—Conventional multiple-input multiple-output (MIMO) technique applied into the millimeter-wave (MMW) and terahertz (THz) imaging applications would suffer from the large number of array elements due to their short wavelengths. In this paper, to reduce the array elements for azimuth-range imaging, a one-dimensional (1-D) sparse MIMO array is introduced, which combines with the wideband emitted signal to achieve 2-D imaging in the near field. Provided with these greatly reduced spatial samples measured by the sparse array, an off-the-grid sparse imaging algorithm is proposed to recover the arbitrarily distributed scatterers in 2-D plane. Particularly, the proposed approach takes advantages of the MIMO geometry and matrix pencil (MP) method. It utilizes the echo in wave-number domain which is featured by the MIMO geometry to make a lossless dimension reduction from the 2-D unknown position of each scatterer into a local 1-D frequency. After estimating those local 1-D frequencies by MP method, a MIMO-structure-determined filter is developed to fulfill the inverse mapping and finally achieve imaging without the pairing problem. Simulations and experiments verify the effectiveness of the proposed approach.

Index Terms—MIMO, sparse array, MMW, THz, near field.

I. INTRODUCTION

Synthesized aperture radar (SAR) technology is of interest in the imaging fields, especially in the security-related applications by adopting millimeter-wave (MMW) and terahertz (THz) bands [1]–[4]. Plenty of classical SAR algorithms are related to Fourier transform (FT), e.g., range-Doppler algorithm (RD), range migration algorithm (RMA), which rigorously require sub-wavelength sampling interval to have a performance guarantee by Nyquist law [5]. This naturally causes the dense spatial sampling and will lead to the heavy system cost in signal acquisition over the MMW and THz bands.

Recently the multiple-input multiple-output (MIMO) technology, which is realized via simultaneous operation of spatially diverse transmit/receive arrays to speed up the signal acquisition, has attracted great attention in microwave imaging,

radar detection, mobile and wireless communication and so on [6]–[9]. Related to MIMO imaging in MMW and THz band, the reference [10] presented an accurate 3-D reconstruction by operating 32 transmitters and 32 receivers in the 100 GHz-MIMO imaging system. The reference [11] proposed a 1×4 MIMO imaging system operating at 90 GHz with 7.5 GHz bandwidth to obtain the resolution of 3.2° in azimuth. A 300 GHz MMW radar system that operates at a stand-off distance of around 7 m is documented in [12] to utilize 8 transmitters and 16 receivers in a bistatic mode. However, among the above mentioned MIMO systems, the array-element spacing in at least one party of the transmitter array and the receiver array is constrained by the sub-wavelength based on Nyquist law. Then, the following spatial convolution between the two arrays would achieve spatially full sampling over the spanned aperture length [13]. This renders the increased scale of arrays to obtain large spanned aperture length for high azimuthal resolution. This situation obviously would be aggravated in the MMW and THz bands due to their short wavelength.

In this paper, we are addressing the above concerns by adopting a 1-D MIMO geometry with both the sparse transmitter array and the sparse receiver array. In such a way, even if a long spanned aperture length is required, the number of the physical array elements would be greatly reduced. Nevertheless, it leads to an under-sampling condition for imaging, which would make the performance loss of FT-based algorithms. Currently, a popular way to deal with the under-determined inversion problem is compressed sensing (CS) [14], [15]. CS-based algorithm tacitly assumes that the scatterers exactly lie on the predefined grids. This obviously violates the nature of scatterers as they are arbitrarily distributed in space. The off-the-grid scatterers thus cause the basis mismatch [16] and make CS-based algorithm less effectiveness [17]. Therefore, we propose an off-the-grid sparse imaging algorithm to achieve the imaging of arbitrary scatterers. The proposed algorithm makes a combination of 1-D MIMO geometry and the spectra estimation technique in such a way that 2-D imaging can rely on 1-D parameter estimation. The unknown 2-D position of each scatterer is firstly one-to-one mapped into a local 1-D frequency by employing the MIMO geometry. Those 1-D local frequencies are then estimated by the matrix-pencil (MP) algorithm, a classical spectrum-estimation algorithm for 1-D continuous parameter estimate. After that, a MIMO-structure-determined filter is developed to fulfill the inverse mapping and finally achieve imaging in the azimuth-range plane.

Furthermore, the Cramer-Rao bound (CRB) is derived to analyze the performance of the proposed algorithm. The proof-

This work was supported in part by the National Program on Key Basic Research Project of China (973 Program) (2014CB339806), in part by the Major National Development Project of Scientific Instrument and Equipment (2012YQ15009205, 2016YFC1202505), in part by the National Natural Science Foundation of China (61605113), in part by the Natural Science Foundation of Shanghai (16ZR1423100), in part by the Shanghai leading talent (2016019), and in part by the Young Yangtze River Scholar. (Corresponding author: Yiming Zhu.)

X. Ding and S. Wu are with the Terahertz Technology Innovation Research Institute, University of Shanghai for Science and Technology, Shanghai 200093, China (e-mail: usstxi@163.com; 2524847186@qq.com).

L. Ding, P. Li and Y. Zhu are with the Terahertz Technology Innovation Research Institute and the Shanghai Key Laboratory, Shanghai 200093, China, and also with the Terahertz Science Cooperative Innovation Center, Shanghai 200093, China (e-mail: sunnylding@usst.edu.cn; 15221338046@qq.com; ymzhu@usst.edu.cn).

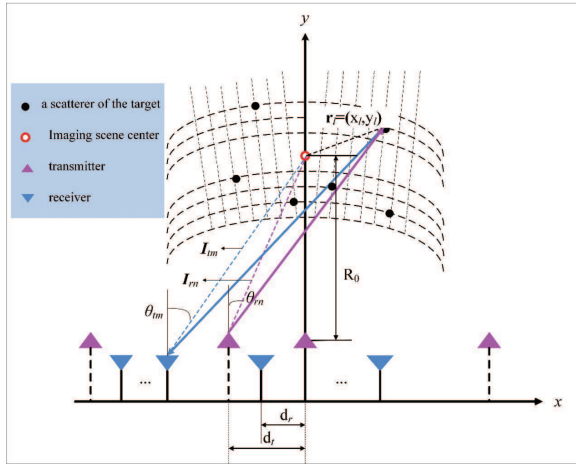


Fig. 1. THz MIMO azimuth-range imaging

of-principle experiments of MIMO geometry are then devised through a time-division-multiplexing-like method. Both the simulations and experiments are conducted in the 26.5 GHz - 40 GHz band. Compared to the FT-based algorithm with different scale of measurements obtained both by MIMO geometry and by monostatic SAR, the results demonstrate the effectiveness and validity of the proposed imaging method.

II. SIGNAL MODEL

The geometry of near-field MIMO imaging system in azimuth-range plane is shown in Fig.1. Without loss of generality, here we adopt the 1-D uniform transmitter- and receiver-array to simplify the analysis. There are M transmitters with the array interval of d_t , and N receivers with the array interval of d_r . Thus the m -th transmitter and the n -th receiver is located at (x_{tm}, R_0) and (x_{rn}, R_0) , respectively, where $x_{tm} = (m-1)d_t - Md_t/2$ and $x_{rn} = (n-1)d_r - Nd_r/2$, R_0 denotes the distance between the baseline of the array and the center of the scene. Conventionally, at least one part of d_t and d_r is constrained to the sub-wavelength by Nyquist law, and this leads to the finally full sampling in the azimuth. It is obvious to have that the corresponding system cost will scale up in the MMW and THz band. Therefore, here we consider the 1-D sparse MIMO array, where both d_t and d_r need not meet the sub-wavelength requirement.

All the transmitted signals are orthogonal to each other. The m -th emitted signal is $s_m(t) = u_m(t)e^{j2\pi f_c t}$ with complex envelope $u_m(t)$ and carrier frequency f_c , $m = 1, \dots, M$. Therefore, assuming that there are L scatterers in the interested scene, the echo at the n -th receiver is

$$y_n(t) = \sum_{m=1}^M \sum_{l=1}^L \sigma(\mathbf{r}_l) s_m(t - \tau_{n,m}(l)) \quad (1)$$

where $n = 1, \dots, N$, $\sigma(\mathbf{r}_l)$ is the complex reflection coefficient of the l -th scatterer whose position is denoted as $\mathbf{r}_l = (x_l, y_l)$, $l = 1, \dots, L$, and $\tau_{n,m}(l)$ is the path delay from the m -th

transmitter to the l -th scatterer and then to the n -th receiver. That is, $\tau_{n,m}(l)$ is of the form as

$$\tau_{n,m}(l) = \frac{\sqrt{(x_{tm} - x_l)^2 + (R_0 - y_l)^2} + \sqrt{(x_{rn} - x_l)^2 + (R_0 - y_l)^2}}{c} \quad (2)$$

where c is the light velocity.

After the down-conversion by multiplying the signal of $e^{-j2\pi f_c t}$, the orthogonal matched filter between the baseband signal at n -th receiver and the m -th transmitted signal yields

$$y_{n,m}(t) = \sum_{l=1}^L \sigma(\mathbf{r}_l) e^{-j2\pi f_c \tau_{n,m}(l)} u_m(t - \tau_{n,m}(l)) \otimes u_m^*(t) \quad (3)$$

Taking the Fourier transform (FT) of (3), we have

$$Y_{m,n}(f) = \mathcal{F}\{y_{m,n}(t)\} = U_m(f) \sum_{l=1}^L \sigma(\mathbf{r}_l) e^{-j2\pi(f_c + f)\tau_{n,m}(l)} \quad (4)$$

where $\mathcal{F}\{u_m(t) \otimes u_m^*(t)\}$ is the power spectral of the m -th waveform with $f \in [0, B]$, and B denotes the bandwidth of each transmitted signal. Since $U_m(f)$ is known, an alternatively concise form of (4), denoted as $z_{n,m}(f)$, is

$$z_{n,m}(f) = \frac{Y_{m,n}(f)}{U_m(f)} = \sum_{l=1}^L \sigma(\mathbf{r}_l) e^{-j2\pi(f_c + f)\tau_{n,m}(l)} \quad (5)$$

Due to the short range between the array and the targets, the exponential term in (5) denotes the spherical wave. The term $\tau_{n,m}(l)$ in (5) can be approximated through Taylor expansion [18], i.e.,

$$\tau_{m,n}(l) \approx \frac{1}{c} \left(\sqrt{x_{tm}^2 + R_0^2} \right) + \left(\sqrt{x_{rn}^2 + R_0^2} \right) - \frac{1}{c} (\mathbf{I}_{tm} + \mathbf{I}_{rn}) \mathbf{r}_l \quad (6)$$

where $\mathbf{I}_{tm} = (\sin \theta_{tm}, \cos \theta_{tm})$, $\mathbf{I}_{rn} = (\sin \theta_{rn}, \cos \theta_{rn})$, θ_{tm} and θ_{rn} are the azimuth angles of the m -th transmitter and the n -th receiver, respectively, as Fig.1 shows. Since the term $\frac{1}{c} \left(\sqrt{x_{tm}^2 + R_0^2} \right) + \left(\sqrt{x_{rn}^2 + R_0^2} \right)$ in (6) is a known quantity independent of targets, it can be easily compensated and will be omitted in the following discussion for simplicity.

By letting $\mathbf{K}_{n,m}(f)$ be $\frac{f_c + f}{c} (\mathbf{I}_{tm} + \mathbf{I}_{rn})$, the signal in (5) then can be further expressed as

$$\begin{aligned} z_{n,m}(f) &= \sum_{l=1}^L \sigma(\mathbf{r}_l) e^{j2\pi \mathbf{K}_{n,m}(f) \mathbf{r}_l} \\ &= \sum_{l=1}^L \sigma(\mathbf{r}_l) e^{j2\pi (K_{n,m}^x(f) x_l + K_{n,m}^y(f) y_l)} \end{aligned} \quad (7)$$

where $\mathbf{K}_{n,m}(f) = (K_{n,m}^x(f), K_{n,m}^y(f))$ denotes a sampling in the wave-number domain. In specific, $K_{n,m}^x(f)$ and $K_{n,m}^y(f)$ are of the forms as

$$\begin{aligned} K_{n,m}^x(f) &= \frac{f_c + f}{c} (\sin \theta_{tm} + \sin \theta_{rn}) \\ K_{n,m}^y(f) &= \frac{f_c + f}{c} (\cos \theta_{tm} + \cos \theta_{rn}) \end{aligned} \quad (8)$$

From (7) we can see that the wave-number-domain echo $z_{n,m}(f)$ and the reflectivity of the scatterer $\sigma(\mathbf{r}_l)$ satisfy the FT relationship. This indicates that a 2-D reflectivity can be obtained by an 2-D inverse FT if the echoes are collected subject to Nyquist law. Obviously in the current case of 1-D sparse MIMO array, this condition is not guaranteed. Besides, CS-based reconstruction suffers from the well-known basis mismatch problem and is hard to reconstruct arbitrarily distributed scatterers. Therefore, to address these problems, an off-the-grid sparse imaging by employing the MIMO geometry and the spectrum-estimation-based high-resolution technique is proposed.

III. OFF-THE-GRID SPARSE IMAGING ALGORITHM

Assuming that the (n, m) -th channel (i.e., the path from the m -th transmitter to the target and then to the n -th receiver) has Q samples in frequency domain, its q -th sample is

$$z_{n,m}(q) = \sum_{l=1}^L \sigma(\mathbf{r}_l) e^{j2\pi(\mathbf{K}_{n,m}^x(q)x_l + \mathbf{K}_{n,m}^y(q)y_l)} \quad (9)$$

where $q = 0, \dots, Q-1$ and the discrete form of (8) is

$$\begin{aligned} K_{n,m}^x(q) &= \frac{f_c + \frac{B}{Q}q}{c} (\sin\theta_{tm} + \sin\theta_{rn}) \\ K_{n,m}^y(q) &= \frac{f_c + \frac{B}{Q}q}{c} (\cos\theta_{tm} + \cos\theta_{rn}) \end{aligned} \quad (10)$$

Recalling the composition of azimuth and frequency sampling in the wave-number domain as (10) shows, we can replace the 2-D position of the l -th scatterer (x_l, y_l) to a 1-D local frequency, denoted as $\beta_{n,m}(\mathbf{r}_l)$, i.e.,

$$\beta_{n,m}(\mathbf{r}_l) = \frac{B}{cQ} q (\mathbf{I}_{tm} + \mathbf{I}_{rn}) \cdot \mathbf{r}_l \quad (11)$$

Thus, (9) can be rewritten into a more compact 1-D form as

$$z_{n,m}(q) = \sum_{l=1}^L \tilde{\sigma}(\mathbf{r}_l) e^{j2\pi q \beta_{n,m}(\mathbf{r}_l)} \quad (12)$$

where $\tilde{\sigma}(\mathbf{r}_l) = \sigma(\mathbf{r}_l) e^{j2\pi \frac{f_c}{c} (\mathbf{I}_{tm} + \mathbf{I}_{rn})^T \cdot \mathbf{r}_l}$.

A. Algorithm

Based on (12), to address the problem of the high-resolution imaging without grid dependence in the under-sampling condition, we take into account the spectrum-estimation technique, e.g., the matrix pencil (MP) algorithm, to estimate $\beta_{n,m}(\mathbf{r}_l)$. The detailed off-the-grid sparse algorithm is depicted as follows, by combing the MP algorithm (i.e., step1-step2) and the MIMO geometry (i.e., step3-step4).

• Step 1: Hankel Matrix Construction

With respect to each transmitter-receiver channel, the echo can be collected as

$$\mathbf{z}_{n,m} = [z_{n,m}(0) \ \cdots \ z_{n,m}(Q-1)]^T \quad (13)$$

Then, the corresponding Hankel matrix of $\mathbf{z}_{n,m}$ can be stacked as follows, denoted as $\mathbf{Z}_{n,m}$

$$\mathbf{Z}_{n,m} = \begin{bmatrix} z_{n,m}(0) & z_{n,m}(1) & \cdots & z_{n,m}(Q-I) \\ \vdots & \vdots & \ddots & \vdots \\ z_{n,m}(I-1) & z_{n,m}(I) & \cdots & z_{n,m}(Q-1) \end{bmatrix} \quad (14)$$

where I is the pencil parameter denoting the window length, each column of $\mathbf{Z}_{n,m}$ is a windowed segment of the matrix sequence $\{z_{n,m}(0), z_{n,m}(1), \dots, z_{n,m}(Q-1)\}$.

• Step 2: Local Frequencies Estimation

The Hankel matrix $\mathbf{Z}_{n,m}$ can be decomposed as follows

$$\mathbf{Z}_{n,m} = \mathbf{U}_s^{n,m} \mathbf{\Sigma}_s^{n,m} \mathbf{V}_s^{n,m} \quad (15)$$

where $\mathbf{U}_s^{n,m}$ and $\mathbf{V}_s^{n,m}$ are the unitary matrices consisting of the eigenvectors of $\mathbf{Z}_{n,m} \mathbf{Z}_{n,m}^H$ and $\mathbf{Z}_{n,m}^H \mathbf{Z}_{n,m}$, respectively, and $\mathbf{\Sigma}_s^{n,m}$ is the diagonal matrix containing the singular values of $\mathbf{Z}_{n,m}$. The superscript $(\cdot)^H$ denotes the conjugate transpose operator.

Let $\mathbf{U}_{s,1}^{n,m}$ and $\mathbf{U}_{s,2}^{n,m}$ be

$$\mathbf{U}_{s,1}^{n,m} = \mathbf{U}_s^{n,m}(1 : Q-I, :) \quad (16)$$

$$\mathbf{U}_{s,2}^{n,m} = \mathbf{U}_s^{n,m}(2 : \text{end}, :) \quad (17)$$

According to the theory of MP, the 1-D local frequencies, i.e., $\{\beta_{n,m}(\mathbf{r}_l); l = 1, 2, \dots, L\}$ are the generalized eigenvalues of $\mathbf{U}_{s,2}^{n,m} - \lambda \mathbf{U}_{s,1}^{n,m}$, denoted as $\{\hat{\beta}_{n,m}(\mathbf{r}_l); l = 1, 2, \dots, L\}$.

• Step 3: Scatterer Position Recovery

(11) builds the relationship between the 2-D position of the scatterers \mathbf{r}_l and its 1-D frequency $\beta_{n,m}(l)$. Therefore, we define a $MN \times 2$ MIMO-structure filter, denoted as \mathbf{W} , and its (n, m) -th row takes the form as

$$\begin{aligned} & [W_{(n,m),1}, W_{(n,m),2}] \\ &= \frac{B}{cQ} [\sin\theta_{tm} + \sin\theta_{rn}, \cos\theta_{tm} + \cos\theta_{rn}] \end{aligned} \quad (18)$$

Then, stacking all the $\hat{\beta}_{n,m}(\mathbf{r}_l)$ as

$$\hat{\beta} = \begin{bmatrix} \hat{\beta}_{1,1}(\mathbf{r}_1) & \cdots & \hat{\beta}_{1,1}(\mathbf{r}_L) \\ \vdots & \ddots & \vdots \\ \hat{\beta}_{N,M}(\mathbf{r}_1) & \cdots & \hat{\beta}_{N,M}(\mathbf{r}_L) \end{bmatrix} \quad (19)$$

The 2-D positions of scatterers $\mathbf{g} = [\mathbf{r}_1, \dots, \mathbf{r}_L]^T$ can be recovered via

$$\mathbf{g} = (\mathbf{W}^H \mathbf{W})^{-1} \mathbf{W}^H \hat{\beta} \quad (20)$$

• Step 4: Complex coefficients recovery

The signal in (12) can be rewritten as

$$z_{n,m}(q) = \mathbf{D}_{n,m}^H(q) \mathbf{H}_{n,m} \boldsymbol{\sigma} \quad (21)$$

where

$$\begin{aligned} \mathbf{D}_{n,m}(q) &= [e^{-j2\pi q \beta_{n,m}(\mathbf{r}_1)}, \dots, e^{-j2\pi q \beta_{n,m}(\mathbf{r}_L)}]^T \\ \mathbf{H}_{n,m} &= \text{diag} \left(e^{j2\pi \frac{f_c}{c} (\mathbf{I}_{tm} + \mathbf{I}_{rn})^T \cdot \mathbf{r}_1}, \dots, e^{j2\pi \frac{f_c}{c} (\mathbf{I}_{tm} + \mathbf{I}_{rn})^T \cdot \mathbf{r}_L} \right) \\ \boldsymbol{\sigma} &= [\sigma(\mathbf{r}_1), \dots, \sigma(\mathbf{r}_L)]^T \end{aligned}$$

Then, $\mathbf{z}_{n,m}$ in (13) can be further expressed as

$$\mathbf{z}_{n,m} = \mathbf{D}_{n,m}^H \mathbf{H}_{n,m} \boldsymbol{\sigma} \quad (22)$$

where

$$\begin{aligned} \mathbf{z}_{n,m} &= [z_{n,m}(0), \dots, z_{n,m}(Q-1)]^T \\ \mathbf{D}_{n,m} &= [\mathbf{D}_{n,m}(0) \cdots \mathbf{D}_{n,m}(Q-1)] \end{aligned}$$

Obviously, (22) shows that the complex coefficients of $\boldsymbol{\sigma}$ can be estimated through solving those linear equations over all channels, i.e.,

$$\hat{\boldsymbol{\sigma}} = \frac{1}{N \times M} \sum \mathbf{H}_{n,m}^{-1} (\mathbf{D}_{n,m} \mathbf{D}_{n,m}^H)^{-1} \mathbf{D}_{n,m} \mathbf{z}_{n,m} \quad (23)$$

where the mean operation is taken over all channels to improve the estimation accuracy.

B. Performance discussion

It can be observed from step 1-step 4 that the estimation performance of the proposed algorithm for arbitrarily distributed scatterers is determined by their local frequencies estimation, i.e., $\{\beta_{n,m}(\mathbf{r}_l)\}$. Therefore, a brief discussion about the estimation variance of $\beta_{n,m}(\mathbf{r}_l)$ in terms of CRB is provided in Appendix A (see [19] for more information).

Then, we can also see from step 1-step 4 that the computation complexity of the proposed algorithm is focused on step 2, related to the matrix decomposition involved in MP method. Based on [19], the computation complexity of the proposed algorithm can be estimated about

$$I^2(Q - I + 1) + \frac{17}{3}I^3 \quad (24)$$

The computational complexity of 2-D FT [20], in comparison, is about

$$\frac{1}{2}(\log_2 Q)Q \quad (25)$$

The ratio of the computational complexity of the proposed algorithm over that of the 2D-FT based method is

$$\frac{I^2(Q - I + 1) + \frac{17}{3}I^3}{\frac{1}{2}(\log_2 Q)Q} \quad (26)$$

which would be examined numerically as a function of parameter I and Q in the Simulation section.

IV. SIMULATION

The theoretical resolution in the azimuth dimension (along the x -axis) and in the range dimension (along the y -axis) are respectively given as

$$\rho_x = \frac{cR}{fMNd_r}, \rho_y = \frac{c}{2B} \quad (27)$$

The parameters of the considered MIMO geometry are set as Table I shows.

TABLE I
THE PARAMETERS OF THE CONSIDERED MIMO RADAR

Parameter	Variable	Value
The length of the array in the x-direction	L_x	0.51m
The distance between the Antenna array baseline and the imaging scene	R_0	0.5m
Center frequency of the transmitted signal	f	35GHz
Wavelength	λ	1.64mm
Spatial spacing by Nyquist law	d^*	0.43cm
Bandwidth	B	13.5GHz
The sampling number in frequency domain	Q	80
Theoretical azimuth resolution by Nyquist law	ρ_x	0.78cm
Theoretical range resolution by Nyquist law	ρ_y	1.11cm

A. Simulations

Here, we compare the proposed algorithm with the traditional FT algorithm and OMP algorithm (a classical algorithm in the CS field).

The estimation error, denoted as E , is calculated as

$$E = \sum_{l=1}^L \frac{1}{L} \|\hat{\mathbf{r}}_l - \mathbf{r}_l\|_2 \quad (28)$$

where $\hat{\mathbf{r}}_l = (\hat{x}_l, \hat{y}_l)$ and $\mathbf{r}_l = (x_l, y_l)$ denote the estimated and the real position of the l -th scatterer, respectively. It is worth noting that to avoid the influence of the mainlobe in FT algorithm, its estimation error is calculated by taking its L peaks.

Firstly, the imaging by 2-D FT-based algorithm under the full data set and under-sampling is tested, respectively, to investigate the influence of sampling on FT performance. In the case of full data set, the receiver spacing is set as $d_r = d^*$, and the transmitter spacing is set as $d_t = Nd^*$, where $d^* = \frac{\lambda}{2}$ denotes the sub-wavelength sampling interval by Nyquist law. In such a way, we can have 4 transmitters and 30 receivers, i.e., $M = 4, N = 30$. In the case of under-sampling, the receiver spacing and the transmitter spacing is set as $d_r = 8d^*$ and $d_t = Nd_r = 64d^*$, respectively, and such that $M = 4, N = 8$. This means that there is under-sampling for a factor of 8. By arbitrarily choosing 6 scatterers in the azimuth-range plane, as shown in Fig.2, the comparison between (a) and (b) represents the failure by FT algorithm in the case of under sampling, and spatial under-sampling makes the ambiguity of imaging in azimuth. Hence, the error in Fig.2.(b) is referred to infinity, denoted as Inf.

Then, under the under-sampling condition, the imaging comparison is taken between OMP and the proposed algorithm. For the same scatterers as that in Fig.2, the imaging results of two algorithms are shown in Fig.3 (a) and (b), respectively. Obviously, it demonstrates that our proposed approach can provide a better imaging than OMP, while the performance of OMP severely depends on the match between the meshgrids and the scatterers positions. Moreover, the comparison between Fig.2 (a) and Fig.3 (b) shows that the proposed algorithm can outperform FT algorithm with the full data set.

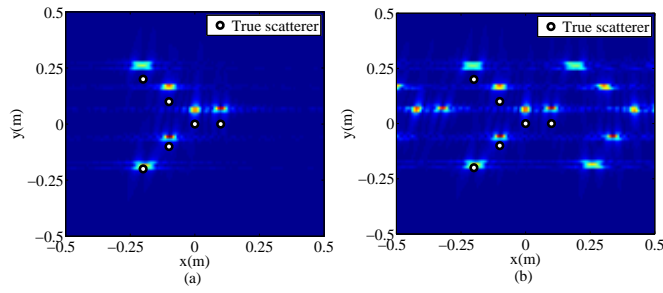


Fig. 2. Image by the FT algorithm: (a) Full data set with $d_r = d_r^*$, $E=0.057\text{mm}$. (b) Under-sampling with $d_r = 8d_r^*$, $E=\text{Inf}$

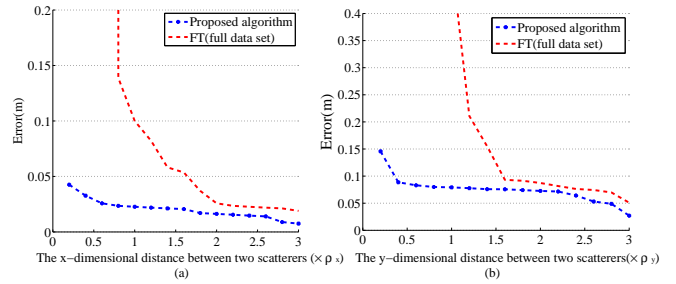


Fig. 4. Imaging performance ($d_r = 8d_r^*$, $M=4$, $N=8$): (a) with the varying of the x-dimensional distance between two scatterers. (b) with the varying of the y-dimensional distance between two scatterers.

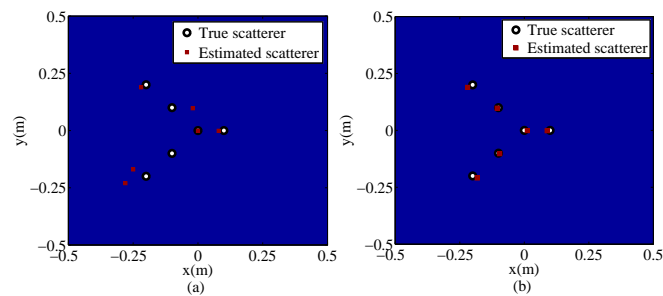


Fig. 3. Under-sampling imaging with $d_r = 8d_r^*$: (a) OMP, $E=0.09\text{ m}$, (b) Proposed algorithm, $E=0.04\text{ m}$.

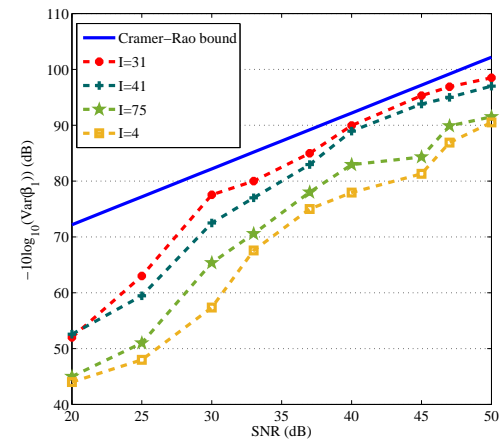


Fig. 5. The inverted sample variance of one frequency β_1 , versus SNR. $Q = 80$

Next, the imaging performance of the proposed algorithm is tested in terms of estimation error E , as shown in Fig.4, where the result by FT with full sampling is taken as a comparison. Fig.4. (a) and (b) illustrate the performance versus the x-dimensional and y-dimensional distance between two scatterers, respectively, and show that the proposed algorithm can attain the theoretical resolution in both dimensions with greatly reduced measurements.

Provided with the CRB in appendix A, here we take one scatterer as an example to test the estimation performance of the algorithm in comparison with its theoretical limit. The parameters are set as $Q = 80$, $(x_1, y_1) = (0.1, 0)$, $\beta_1 = 0.015$, $\bar{\sigma}_1 = 1$. Fig.5 shows the estimation variance of β_1 with respect to the varying signal-to-noise (SNR). The definition of SNR is given in appendix A. It is clear from Fig.5 that the estimation accuracy would be improved with the increase of SNR. The different curves with respect to different value of I indicates that the parameter I works as a tuning parameter which can be adjusted to increase the estimation accuracy. When $I = 31$, i.e., approximately one third of Q , the estimation variance can come close to its CRB, and this is consistent with the analysis in [19] and [20].

In Fig.6, the computation complexity of the proposed algorithm is examined with varying I and Q . The ratio in (30) is compared with a certain threshold, where the result corresponding to the ratio less than the threshold is set as 1, otherwise is set as 0. It is obvious to observe from Fig.6 that the proposed algorithm has a higher computation complexity than its counterpart FT-based algorithm. This result is quite reasonable and well-known due to the matrix-decomposition property of spectrum-estimation technique. However, from

Fig.6.(a), (b) and (c), where the threshold is set as 10, 50, and 100, respectively, it can be seen that as Q (i.e., the number of samples) increases, the range of I will be expanded for acceptable complexity of the proposed algorithm. In other words, the more the number of samples is, the greater the range of I can be. Due to the relative small I compared with the size of data Q , it should be noted that the proposed algorithm is suitable for the scene with small size of data set. However, it is worth noting that to reduce the size of data set is the original intension of the presented article, and thus our proposed algorithm is efficient and of practical application to some extent. Besides, Fig.6 (d) shows that if the requirement on computational complexity can be somehow relaxed, the range of I would increase. This means that the detection performance of the proposed algorithm can be improved.

B. Experimental Results

Assuming that the under-the-test targets are static, the multiple input and multiple output of MIMO geometry is simulated by a single input and a single output through a time-division-multiplexing-like method, as shown in Fig.7. That is, two channels of the VNA are taken as the input, denoted as TX and the output, denoted as RX of MIMO, respectively. The multiple inputs and multiple outputs are collected at different time and different spatial positions by moving TX and RX

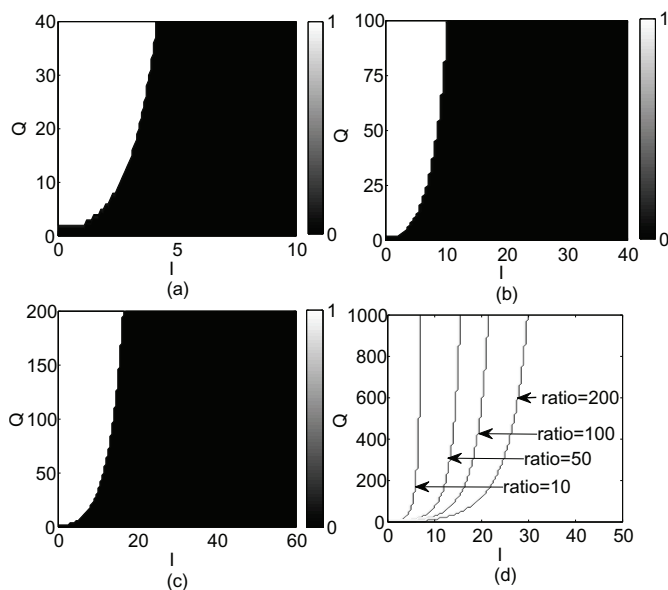


Fig. 6. Computational complexity:(a) the ratio threshold is 10. (b) the ratio threshold is 50. (c) the ratio threshold is 100. (d) the boundaries with respect to four different ratio thresholds.

along the linear trail. The 3 dB beamwidth of the antennas is 30° . The distance between the linear trail and the center of scene is 0.25 m (i.e., R_0), and other parameters are set the same as that in Table 1.

Firstly, the imaging results are checked by the proposed algorithm and FT under the full data set, shown in Fig.8. The targets are two metal cylinders, as Fig.8 (a) shows. It is found from (b) and (c) that, the proposed algorithm has better imaging performance, while the FT algorithm would expand the reconstructed scatterer due to the mainlobe of point spread function (PSF). As shown in (d), the shape of PSF is unpleasing partially because of the limited beamwidth of the adopted antennas.

The comparison between OMP and the proposed method is conducted under the condition of the full data set and partial data set, respectively. The targets are multiple metals cylinders, shown in Fig.9 (a). It is found from (b) and (c) that our proposed approach outperforms OMP under full data set. Then for the case of under-sampling, as shown in Fig.10, we can see that OMP is hard to achieve the imaging due to the mismatch problem of the uniform meshgrids and the arbitrary positions of the scatterers, but the proposed algorithm can maintain a good imaging performance.

Then, for the same scene of interest, the imaging of FT based on monostatic SAR and on MIMO are compared to discuss the influence of geometry difference on imaging performance. The experiment of near-field SAR imaging system is shown in Fig.11. The synthesized aperture length is as the same as that in MIMO. The imaging result by SAR and by MIMO is shown in Fig.12 (a) and (b), respectively. It is obvious to have that the imaging performance by MIMO geometry is much better than that by monostatic SAR. There are some aspects to affect the performance of monostatic SAR in our experiment. The limited beamwidth of antenna is one

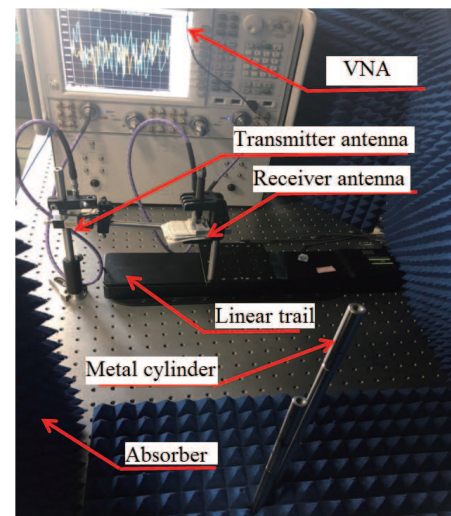


Fig. 7. Photograph of the MIMO imaging system

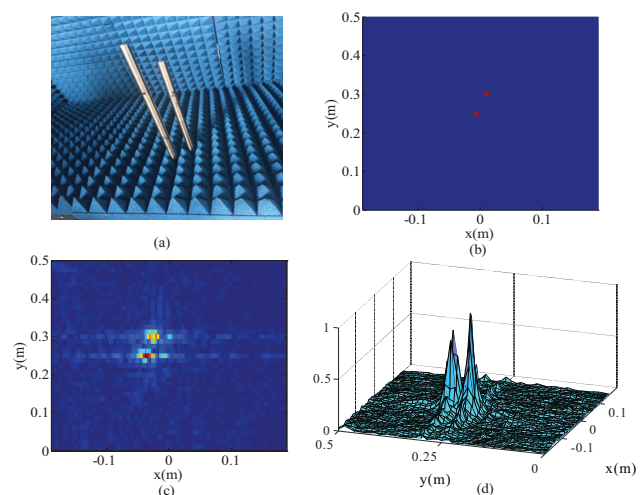


Fig. 8. Imaging results of two metal cylinders in MIMO ($d_r = d_r^*$) (a) Photograph of two metal cylinders and the distance is 2.5 cm in the x direction and 5 cm in the y direction (b) Image by the proposed algorithm. (c) 2-D image by FT (d) 3-D image by FT

negative factor, and it constraints the efficient field of view of SAR. Another possible factor is that the effective scattering area of the metal cylinder is too small to make an effectively receiving by monostatic SAR. However, MIMO geometry due to the multiple illumination and the multiple receiving can have the spatial diversity gain to bring back more information of the scatterers, and can maintain a good imaging in the face of limited beamwidths and the small scattering area of targets.

V. CONCLUSION

An off-the-grid-sparse imaging algorithm based on 1-D MIMO sparse array has been proposed for MMW and THz near-field imaging. The sparse MIMO geometry adopts the sparse arrays both in transmitting and receiving to make a decrease in physical array elements, while the imaging performance is then maintained by the proposed off-the-grid sparse imaging algorithm. The proposed algorithm makes use

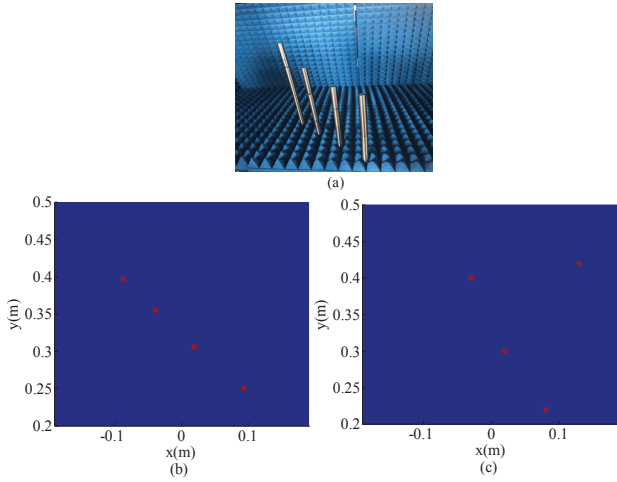


Fig. 9. Imaging results of four metal cylinders based on MIMO geometry ($d_r = d_r^*$) (a) Photograph of four metal cylinders and the distance is 5 cm in the x direction and 10 cm in the y direction (b) Imaging by the proposed algorithm (c) Imaging by OMP

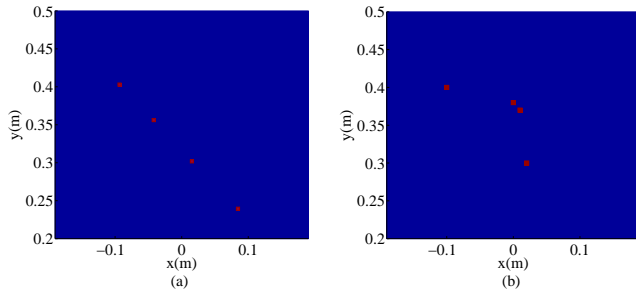


Fig. 10. Imaging results of four metal cylinders based on MIMO geometry ($d_r = 8d_r^*$) (a) Imaging by the proposed algorithm (b) Imaging by OMP

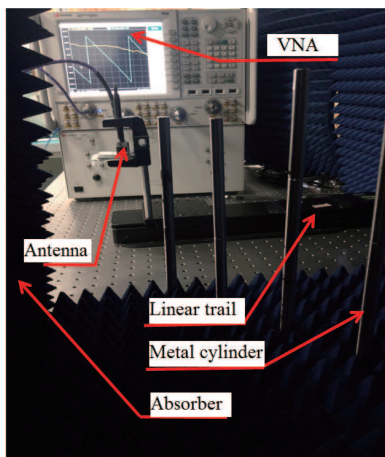


Fig. 11. Photograph of the SAR imaging system

of MIMO geometry and the matrix pencil (MP). These two combine in such a way that 2-D imaging of arbitrarily distributed scatterers is achieved by a 1-D continuous parameter estimation method. Benefited from the high-resolution technique of MP, the originally limited information of the targets involved in the reduced samples can be enhanced to guarantee

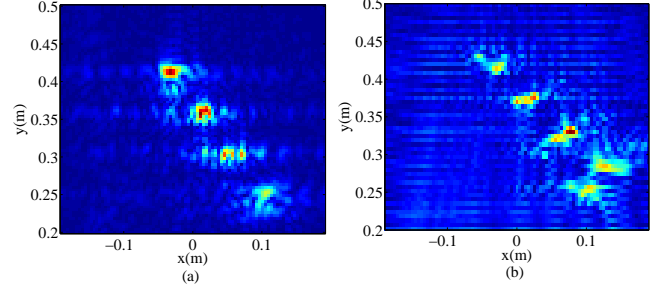


Fig. 12. Imaging results of four metal columns in different imaging system ($d_r = d_r^*$) (a) Imaging by FT based on MIMO geometry. (b) Imaging by FT based on monostatic SAR

the estimation performance. Then, the inverse mapping from 1-D parameter to 2-D position is based on the solution of a series of linear equations and thus avoids the pairing problem. The validity of the sparse MIMO geometry and the proposed algorithm has been demonstrated by simulations and experiments. The results show that MIMO geometry can have the spatial diversity gain to address the problem of the limited beamwidth of the antennas and the small scattering surface of the targets. Besides, although the proposed algorithm would suffer from the heavy computational complexity for large scene, some relaxation in computation complexity can increase the feasibility and the practicability of off-the-grid sparse imaging for MMW/THz MIMO near-field application.

APPENDIX A

Here, we derive a Fisher information matrix whose elements make it easy to see the relationship between CRB and the parameters. From (12), we can write

$$y(q) = z(q) + w(q) = \sum_{l=1}^L \tilde{\sigma}_l e^{j2\pi q \beta_l} + w(q) \quad (29)$$

where $w(q)$ is a Gaussian white noise with mean 0 variance δ^2 . The SNR is defined as follows:

$$SNR(dB) = 10 \log_{10} \frac{\sum_{q=0}^{Q-1} y^2(q)}{Q \delta^2} \quad (30)$$

For simplicity, we can rewrite (29) as

$$s = z + w \quad (31)$$

where $\mathbf{s} = [s_0, s_1, \dots, s_{Q-1}]^T$ and $\mathbf{z} = [z_0, z_1, \dots, z_{Q-1}]^T$. If the probability density function (pdf) of \mathbf{w} is normal, i.e., $W(\mathbf{0}, 2\delta^2 I_Q)$ then the pdf of \mathbf{s} is $W(\mathbf{z}, 2\delta^2 I_Q)$. It is clear that the mean vector \mathbf{z} depends on the parameter vector $\boldsymbol{\theta}$ defined as

$$\boldsymbol{\theta} = [\boldsymbol{\theta}_1^T, \dots, \boldsymbol{\theta}_L^T]^T \quad (32)$$

$$\boldsymbol{\theta}_l = [\tilde{\sigma}_l, \beta_l]^T \quad (33)$$

Let θ_l denote the l -th element of $\boldsymbol{\theta}$. Then the (l, j) -th element of the Fisher information matrix \mathbf{J} can be shown as

$$(\mathbf{J})_{l,j} = 1/\delta^2 \sum_{q=1}^{Q-1} \text{Re} \{ (dz_q/d\theta_l)(dz_q^*/d\theta_j) \} \quad (34)$$

where $d()/d\theta_l$, is partial derivative. But \mathbf{J} can be partitioned as

$$\mathbf{J} = \{\mathbf{J}_{l,j}; l, j = 1, 2, \dots, L\} \quad (35)$$

where $\mathbf{J}_{l,j}$ is a 2×2 (l, j)-th block matrix of \mathbf{J} , which can be shown from (29) to be

$$\mathbf{J}_{l,j} = 1/\delta^2 \mathbf{B}_l \text{Re} \{ \mathbf{C}_{l,j} \} \mathbf{B}_j \quad (36)$$

In which

$$\mathbf{B}_l = \text{diag} \{1, \tilde{\sigma}_l\} \quad (37)$$

$$\mathbf{C}_{l,j} = \begin{bmatrix} \rho_{i,j,0} & -j\rho_{i,j,1} \\ j\rho_{i,j,1} & \rho_{i,j,2} \end{bmatrix} \quad (38)$$

$$\rho_{i,j,0} = \sum_{q=0}^{Q-1} (c_l \cdot c_j^*)^q \quad (39)$$

$$\rho_{i,j,1} = \sum_{q=0}^{Q-1} q(c_l \cdot c_j^*)^q \quad (40)$$

$$\rho_{i,j,2} = \sum_{q=0}^{Q-1} q^2(c_l \cdot c_j^*)^q \quad (41)$$

Furthermore, we can write

$$\mathbf{Z}_{l,j} = \text{Re} \{ \mathbf{C}_{l,j} \} \quad (42)$$

Then the 2×2 (l, j)-th block matrix of \mathbf{J}^{-1} can be shown to be

$$\mathbf{J}_{i,j}^{-1} = \delta^2 \cdot \mathbf{B}_j^{-1} \cdot \mathbf{Z}_{l,j}^{-1} \cdot \mathbf{B}_l^{-1} \quad (43)$$

Then the l -th diagonal block matrix of \mathbf{J}^{-1} is

$$\mathbf{J}_{l,l}^{-1} = \delta^2 \cdot \mathbf{B}_l^{-1} \cdot \mathbf{Z}_{l,l}^{-1} \cdot \mathbf{B}_l^{-1} \quad (44)$$

Then, the two diagonal elements of $\mathbf{J}_{l,l}^{-1}$ denote the C-R bounds for $\tilde{\sigma}_l$ and β_l , respectively.

REFERENCES

- [1] M. Aoki, S. R. Tripathi, M. Takeda, and N. Hiromoto, "Passive imaging and emissivity measurement with a 4k-cryocooled Terahertz photoconductive detector," *Ieice Electronics Express*, vol. 9, no. 5, pp. 333–338, 2012, [doi:10.1587/elex.9.333].
- [2] T. Li and L. Du, "Target discrimination for SAR atr based on scattering center feature and k-center one-class classification," *IEEE Sensors Journal*, pp. 1–1, 2018, [10.1109/JSEN.2018.2791947].
- [3] S. Caorsi, M. Donelli, A. Lommi, and A. Massa, "Location and imaging of two-dimensional scatterers by using a particle swarm algorithm," *Journal of Electromagnetic Waves & Applications*, vol. 18, no. 4, pp. 481–494, 2004, [doi:10.1163/156939304774113089].
- [4] M. Soumekh, "A system model and inversion for synthetic aperture radar imaging," *IEEE Transactions on Image Processing A Publication of the IEEE Signal Processing Society*, vol. 1, no. 1, pp. 64–76, 1992, [doi:10.1109/icassp.1990.115861].
- [5] D. M. Sheen and T. E. Hall, "Reconstruction techniques for sparse multistatic linear array microwave imaging," in *SPIE Defense + Security*, 2014, p. 90780I, [doi:10.1117/12.2053814].
- [6] J. Li and P. Stoica, *MIMO Radar Signal Processing*. Wiley-IEEE Press, 2009, [doi:10.1002/9780470391488].
- [7] W. Q. Wang, "Large time-bandwidth product MIMO radar waveform design based on chirp rate diversity," *IEEE Sensors Journal*, vol. 15, no. 2, pp. 1027–1034, 2014, [doi:10.1109/JSEN.2014.2360125].
- [8] P. S. Kildal and K. Rosengren, "Correlation and capacity of mimo systems and mutual coupling, radiation efficiency, and diversity gain of their antennas: simulations and measurements in a reverberation chamber," *IEEE Communications Magazine*, vol. 42, no. 12, pp. 104–112, 2004, [doi:10.1109/MCOM.2004.1367562].
- [9] L. Xiao, T. Chen, G. Han, W. Zhuang, and L. Sun, "Game theoretic study on channel-based authentication in mimo systems," *IEEE Transactions on Vehicular Technology*, vol. 66, no. 8, pp. 7474–7484, 2017, [doi:10.1109/TVT.2017.2652484].
- [10] J. Moll, M. Kotiranta, B. Hils, and V. Krozer, "A 100 GHz millimeter wave radar system with 32 transmitters and 32 receivers for space applications," in *Radar Conference*, 2013, pp. 687–690, [doi:10.23919/eumc.2012.6459431].
- [11] R. Herschel, S. Nowok, P. Warok, R. Zimmermann, S. A. Lang, and N. Pohl, "MIMO system for fast imaging at 90 GHz," in *Microwave Conference*, 2015, [doi:10.1109/eumc.2015.7345793].
- [12] J. Moll, P. Schops, and V. Krozer, "Towards three-dimensional millimeter-wave radar with the bistatic fast-factorized back-projection algorithm?potential and limitations," *IEEE Transactions on Terahertz Science & Technology*, vol. 2, no. 4, pp. 432–440, 2012, [doi:10.1109/TTHZ.2012.2199113].
- [13] G. P. De and L. Deck, "Three-dimensional imaging by sub-nyquist sampling of white-light interferograms," *Optics Letters*, vol. 18, no. 17, pp. 1462–4, 1993, [doi:10.1364/OL.18.001462].
- [14] M. F. Duarte and R. G. Baraniuk, "Spectral compressive sensing," *Applied & Computational Harmonic Analysis*, vol. 35, no. 1, pp. 111–129, 2013, [doi:10.1016/j.acha.2012.08.003].
- [15] T. Strohmer and B. Friedlander, "Analysis of sparse MIMO radar," *Applied & Computational Harmonic Analysis*, vol. 37, no. 3, pp. 361–388, 2014, [doi:10.1016/j.acha.2013.12.005].
- [16] Y. Chi, L. L. Scharf, A. Pezeshki, and A. R. Calderbank, "Sensitivity to basis mismatch in compressed sensing," *IEEE Transactions on Signal Processing*, vol. 59, no. 5, pp. 2182–2195, 2011, [doi:10.1109/TSP.2011.2112650].
- [17] G. Tang, B. N. Bhaskar, P. Shah, and B. Recht, "Compressed sensing off the grid," *IEEE Transactions on Information Theory*, vol. 59, no. 11, pp. 7465–7490, 2013, [doi:10.1109/TIT.2013.2277451].
- [18] H. Xie, H. Zhao, and Q. Fu, "Taylor expansion and its application in missile-borne sar imaging," in *Synthetic Aperture Radar, 2009. Apsar 2009. Asian-Pacific Conference on*, 2010, pp. 426–430, [doi:10.1109/APSAR.2009.5374291].
- [19] Y. Hua and T. K. Sarkar, "Matrix pencil method for estimating parameters of exponentially damped undamped sinusoids in noise," *IEEE Trans Assp*, vol. 38, no. 5, pp. 814–824, 1990, [doi:10.1109/29.56027].
- [20] T. K. Sarkar and O. Pereira, "Using the matrix pencil method to estimate the parameters of a sum of complex exponentials," *IEEE Antennas & Propag Mag*, vol. 37, no. 1, pp. 48–55, 1995, [doi:10.1109/74.370583].